SIAM J. SCI. COMPUT.
Vol. 25, No. 1, pp. 104–126

ACCURACY OF SPECTRAL AND FINITE DIFFERENCE SCHEMES IN 2D ADVECTION PROBLEMS*

VOLKER NAULIN† AND ANDERS H. NIELSEN†

Abstract. In this paper we investigate the accuracy of two numerical procedures commonly used to solve 2D advection problems: spectral and finite difference (FD) schemes. These schemes are widely used, simulating, e.g., neutral and plasma flows. FD schemes have long been considered fast, relatively easy to implement, and applicable to complex geometries, but are somewhat inferior in accuracy compared to spectral schemes. Using two study cases at high Reynolds number, the merging of two equally signed Gaussian vortices in a periodic box and dipole interaction with a no-slip wall, we will demonstrate that the accuracy of FD schemes can be significantly improved if one is careful in choosing an appropriate FD scheme that reflects conservation properties of the nonlinear terms and in setting up the grid in accordance with the problem.

Key words. numerical simulation, accuracy, fluid, no-slip boundary conditions

AMS subject classifications. 76D05, 65M70, 65M06, 76F40

DOI. 10.1137/S1064827502405070

1. Introduction.

The solution of nonlinear advection problems by numerical means is a well-established procedure used either to augment analytical results or to obtain results when there is no analytical solution at hand. The advection problem appears in a broad context of physical problems, from pure fluid applications and magneto-hydrodynamics of space plasmas to electromagnetic turbulence in magnetically confined fusion plasmas. For many systems the convection is driven by some instability, which saturates into turbulence in the presence of dissipation. It is sometimes argued that accuracy in the evaluation of the convective nonlinearity can be sacrificed in favor of the stability and robustness of the code, properties often achieved by dynamically adjusting local smoothing operators to avoid the creation of small scales not resolved by the finite resolution of the scheme. However, in a number of problems the accurate modeling of the flow of energy between different scales is rather important, as this can crucially influence the evolution of structures in the turbulence as, e.g., global shear flows. These structures drastically affect properties of the turbulence, such as transport, and their accurate modeling is therefore of importance.

Spectral methods for unbounded (periodic) squared domains using Fourier modes have been used for some decades now. These methods have the advantage that they converge fast toward the solution as the number of modes is increased—the so-called spectral convergence. The same fast convergence can be obtained for bounded flows using expansion functions such as Chebyshev polynomials [3, 4]. Our goal in this paper is to compare results obtained from two different classes of finite difference (FD) schemes with results from spectral schemes, with a focus on the high Reynolds number regime.

*Received by the editors April 8, 2002; accepted for publication (in revised form) January 28, 2003; published electronically September 9, 2003. This work was supported by Danish Center for Scientific Computing (DCSC) grant CPU-1101-08 and by INTAS 00-292.

http://www.siam.org/journals/sisc/25-1/40507.html

†Optics and Fluid Dynamics Department, Association EURATOM - Risø National Laboratory, DK-4000 Roskilde, Denmark (volker.naulin@risoe.dk, anders.h.nielsen@risoe.dk).

We consider the following two different FD discretizations of the nonlinearity: one classical going back to Arakawa [1] and a modern third order essentially nonoscillatory (ENO) central scheme as suggested by Kurganov and Levy [15]. For any energy conserving FD discretization of the nonlinearity the viscous damping of small structures has to be faster than the speed by which the nonlinearity creates these small scales in order for the scheme to be stable. ENO and upwind schemes, however, avoid the creation of grid scale structures intrinsically by switching between different discretizations of the differential operators and possibly employing a limiting function on the flux. One should note that this leads to numerical viscosity acting on the grid length-scale that has some resemblance to the method used in so-called large eddy simulations (LES). In LES the turbulence on scales finer than the grid scale is basically modeled as a damping of the larger structures. However, attempts to combine upwind and LES methodologies showed that the combination does not have significant advantages over LES used with centered FDs [18].

Here, we first demonstrate that even for high Reynolds numbers FD schemes can, with good accuracy, produce the detailed evolution of convection problems. We will discuss the necessary ingredients for this—mainly the appropriate choice of grid points and conservation properties of the numerical schemes. Another motivation for benchmarking these different numerical schemes is to compare their behaviors under the implementation of nontrivial boundary conditions. For two different boundary conditions, periodic and no-slip, we have chosen model problems, which have recently been investigated using spectral methods. A more detailed description of the setup of these problems can be found in [9, 12, 20]. Both problems demand high accuracy at these high Reynolds numbers, stressing the nonlinear nature of the advection problem.

The paper is organized as follows. In section 2 we briefly discuss the underlying model. The FD schemes will be described in section 3.

Special attention will be given to the implementation of no-slip boundary conditions. In section 4 we describe the spectral schemes based on Fourier modes, for periodic domains, and Chebyshev polynomials/Fourier modes for the case where one of the coordinates is bounded by no-slip walls.

In section 5 we display our results. For the periodic case we study the merging of two equally signed Gaussian monopoles. In the bounded case we study the dipole-wall interaction in a periodic annulus geometry. Both situations pose a different set of difficulties to the codes, as fine scale vorticity sheets are created by either vortex-vortex or vortex-wall interaction. We will not only discuss overall error estimates but also perform a detailed pointwise comparison of the solutions obtained using the different schemes, as this gives better insight into the accuracy of the solution.

2. Navier–Stokes equations. We consider the 2D, unforced, incompressible Navier–Stokes equations

$$\frac{\partial \vec{v}}{\partial t} + (\vec{v} \cdot \nabla)\vec{v} = \nu \nabla^2 \vec{v} - \nabla p, \tag{2.1}$$

with the incompressibility condition

$$\nabla \cdot \vec{v} = 0. \tag{2.2}$$

Here p is the kinematic pressure, $\vec{v} = (u, v)$ is the 2D flow velocity, and ν the kinematic viscosity. Equations (2.1) and (2.2) have to be solved using appropriate boundary conditions. These can be easily formulated in terms of the velocities but are difficult to express in terms of the pressure or the vorticity.

Taking the rotation of (2.1) transforms it into the vorticity-stream function formulation

$$\frac{\partial \omega}{\partial t} + [\omega, \psi] = \nu \nabla^2 \omega, \tag{2.3}$$

where $\omega \equiv (\nabla \times \vec{v}) \cdot \hat{z}$ is the pseudoscalar vorticity, ψ ($\nabla\psi \times \hat{z} \equiv \vec{v}$) is the stream function, and [.,.] denotes the Jacobian. The stream function is related to the vorticity by the Poisson equation

$$\nabla^2 \psi = -\omega. \tag{2.4}$$

This formulation has the advantage that the pressure, p, is absent from the equations. Furthermore it is a scalar equation, as opposed to the vector equation (2.1).

In order to solve (2.3)–(2.4) we have to apply boundary conditions. For a periodic domain these conditions are trivial. For bounded domains the boundary conditions are usually far from simple. In the case considered here we use a periodic annulus with inner boundary $r^- = A - 1$ and outer boundary $r^+ = A + 1$ with $A = 1.5$. The azimuthal direction is periodic. In the radial direction we apply no-slip boundary conditions, e.g.,

$$v_r \mid_{r=r^\pm} = 0 \quad \text{and} \quad v_\theta \mid_{r=r^\pm} = 0, \tag{2.5}$$

or in terms of the stream function,

$$\nabla\psi \mid_{r=r^\pm} = (0, 0). \tag{2.6}$$

One of these two sets of conditions can be applied directly to the Poisson equation, (2.4), whereas the other set of conditions has to be applied to the discretized form of (2.3), resulting in a Helmholtz equation. Note that the boundary conditions for the quantity ω inferred from the stream function are not trivial. The corresponding conditions originating from different approaches to the problem will be discussed in sections 3 and 4.

To ease comparison and restrict it to the spatial discretization used we employ the same timestep algorithm for all codes, a third order "stiffly stable" scheme as described in [13]. The convection term is evaluated explicitly, while the viscous/diffusive term is treated implicitly. The viscous operator splitting is necessary, as it is well known that the use of explicit schemes with an operator containing an even number of derivatives poses severe restrictions on the timestep, as numerical instabilities have to be avoided.

2.1. Temporal evolution of global quantities. In the absence of viscosity and physical walls, (2.3)–(2.4) possess an infinite number of conserved quantities, including the energy, E, and enstrophy, Ω:

$$E \equiv \frac{1}{2} \int_D \vec{v}^2 \, dA, \tag{2.7}$$

$$\Omega \equiv \frac{1}{2} \int_D \omega^2 \, dA. \tag{2.8}$$

In the presence of viscosity and physical boundaries the time evolution of energy and vorticity is obtained from (2.1)–(2.4) via multiplying (2.3) by ψ and ω, respectively, and subsequent integration over the domain:

$$\frac{dE}{dt} = -\nu \Omega(t) \tag{2.9}$$

and

$$\frac{d\Omega}{dt} = 2\nu \int_{\partial D} \omega \nabla\omega \cdot \hat{n} ds - 2\nu \int_D (\nabla\omega)^2 \, dA, \tag{2.10}$$

where $\hat{n}$ is the outgoing normal to the boundary. We have assumed that the wall velocities are zero and that therefore the energy in (2.9) will always decay. However, the boundary can act as a source of vorticity, as the first term on the right-hand side of (2.10) can be positive. Note that in case of periodic boundary conditions this term will vanish and enstrophy will consequently decay in time.

In order to check the accuracy of our numerical solutions, we have included global error estimates based on these integral quantities. Let F denote either E or Ω; at fixed time intervals we calculate a time-centered, fourth order accurate value of the time derivative of F, denoted $(dF/dt)_{\text{num}}$, by evaluating F at five sequential timesteps. By employing a fourth order estimation, we ensure consistency in approximation level with the third order accurate, stiffly stable time integration scheme [13]. This numerical time derivative is compared to the theoretical value $(dF/dt)_{\text{theor}}$ evaluated from the instantaneous fields entering on the right-hand sides of (2.9)–(2.10). As an error estimate, δF, we employ the relative difference per time unit of these two time derivatives values, so

$$\delta F(t) = \left| \frac{(dF/dt)_{\text{num}} - (dF/dt)_{\text{theor}}}{F(t)} \right|. \tag{2.11}$$

This function is evaluated in our schemes and used to compare the accuracy of the simulations with different resolutions and different schemes.

One should note that these global errors only reflect the conservation properties of the nonlinear term. The Arakawa and Fourier spectral schemes *exactly* conserve energy and enstrophy for zero viscosity. Thus the calculated error will include only time-stepping errors, errors in evaluating the viscosity related terms, and errors due to finite number precision. For the ENO scheme, as well as the Chebyshev–Fourier spectral scheme, this will be different, as the ENO discretization of the nonlinear term does not have the built-in conservation property for quadratic integral invariants. Thus, the error as defined above will, for the ENO case, be a measure of the amount of dissipation introduced by the discretization.

3. FD schemes. The FD discretization of partial differential equations for numerical purposes has a long tradition. FD schemes are usually relatively easy to implement, rather fast, and adaptable to complex geometries and boundary conditions. A drawback is that they offer only limited accuracy, as they approximate derivatives using a finite local stencil. In past years there has been widespread activity in the construction of so-called modern algorithms for the numerical solution of nonlinear conservation laws; see, e.g., [16, 5, 19]. These activities are often connected with the problems of shocks in compressible flows, but the methods are also applied to incompressible flow dynamics [23].

3.1. Discretization of the nonlinearity. A main ingredient in solving (2.3) is the evaluation of the Jacobian. This quadratic nonlinearity produces new scales that might not be representable on the finite resolution grid underlying the numerical computation. An accurate representation of this term is therefore of utmost importance. Here we will use two different FD versions of the nonlinearity following different philosophies on how to treat the appearance of nonresolved structures produced by the nonlinearity.

In his classical paper from 1966, Arakawa [1] introduced a discretization of the Jacobian type of nonlinearity that not only is accurate to third order in space discretization, h, (the error is of order h^4), but also respects that circulation, energy, and enstrophy are conserved under the action of the nonlinearity. These conservation properties determine the redistribution of the energy between different length-scales. Here we use the discretization given as (46) in [1], which we will write down for completeness for $dx = dy = h$:

(3.1)
$$\begin{aligned}[\omega,\psi] = -\frac{1}{12h^2}[&(\psi_{i,j-1} + \psi_{i+1,j-1} - \psi_{i,j+1} - \psi_{i+1,j+1})(\omega_{i+1,j} + \omega_{i,j}) \\ &- (\psi_{i-1,j-1} + \psi_{i,j-1} - \psi_{i-1,j+1} - \psi_{i,j+1})(\omega_{i,j} + \omega_{i-1,j}) \\ &+ (\psi_{i+1,j} + \psi_{i+1,j+1} - \psi_{i-1,j} - \psi_{i-1,j+1})(\omega_{i,j+1} + \omega_{i,j}) \\ &- (\psi_{i+1,j-1} + \psi_{i+1,j} - \psi_{i-1,j-1} - \psi_{i-1,j})(\omega_{i,j} + \omega_{i,j-1}) \\ &+ (\psi_{i+1,j} - \psi_{i,j+1})(\omega_{i+1,j+1} + \omega_{i,j}) \\ &- (\psi_{i,j-1} - \psi_{i-1,j})(\omega_{i,j} + \omega_{i-1,j-1}) \\ &+ (\psi_{i,j+1} - \psi_{i-1,j})(\omega_{i-1,j+1} + \omega_{i,j}) \\ &- (\psi_{i+1,j} - \psi_{i,j-1})(\omega_{i,j} + \omega_{i+1,j-1})].\end{aligned}$$

This discretization of the convective term exactly conserves energy, enstrophy, and circulation. Thus, as smaller scales are produced by the nonlinearity, the numerical solution can be correct only as long as dissipation removes energy at the scale of the grid resolution faster than the nonlinear term transports energy into these scales. Note that generalizations to anisotropic grids ($dx \neq dy$) or nonequidistant grids ($dx, dy \neq constant$) can often be easily derived using the analytical form of [A, B] with appropriate variable transformations before discretization. If this is not possible, there exist generalizations of the Arakawa scheme as found in [19].

Harten et al. [11] introduced the ENO technique in 1987. Its goal is to prevent spurious oscillations in the solution of the advection problem in a robust way; that means the technique is made not to produce new local maxima or minima. Spurious high amplitude oscillations on the grid scale are usually observed in FD schemes as a result of insufficient resolution. ENO schemes monitor the smoothness of the underlying velocity functions and switch to a one-sided lower order representation of the differential operators in the presence of a "discontinuity," e.g., a steep gradient, which ensures that no oscillations on the scale of the underlying grid are produced. We have implemented a third order ENO scheme based on a piecewise continuous polynomial interpolation with central weights in the semidiscrete form, as described in broad detail in [14].

3.2. Nonequidistant grid. In the case of the annular domain ($A - 1 \leq r \leq A + 1$, $0 \leq \theta \leq 2\pi$) with no-slip walls at $r = A \pm 1$, the largest gradients are likely to develop near the walls. It is therefore useful to increase the numerical resolution at the boundary. One way to increase the resolution in the vicinity of the walls is by using the Chebyshev collocation points, located at $r_i = \cos(\pi i/M) + A$. With this choice of collocation points the grid in the interior of the domain becomes only slightly deformed. Note that for fitting an arbitrary function, which is at least $M + 1$ times differentiable in the interval $\{-1 : 1\}$, by a polynomial of degree M, the Chebyshev polynomial of order M will minimize the ∞-norm of the error, according to the *Chebyshev minimal amplitude theorem*; see [3]. According to this theorem

the choice of Chebyshev polynomials as expansion functions for a spectral code on a bounded domain will thus be the most accurate. In the FD case differential operators are discretized by using a finite stencil, fitting as in the ENO scheme a lower order polynomial. The scheme is consequently of fixed order in space, compared to a spectral scheme where the order of approximation increases as the grid spacing is refined, resulting in spectral accuracy. However, we still need a grid that is dense near the wall and has a smooth transition to a nearly equidistant grid in the interior of the domain. The Chebyshev collocation points conveniently satisfy both criteria.

Since we need to evaluate derivatives on the boundaries and utilize ghost points outside the integration domain in order to enforce the boundary conditions, the Chebyshev collocation points are not directly usable, as the distance between them goes to zero at the boundaries. We thus map the equidistantly sampled domain, denoted by the variable x on the interval $\{-1, 1\}$ of Chebyshev collocation points. Subsequently we stretch this to real physical coordinates (denoted r) as follows:

$$r = \frac{r^+ - r^-}{x^+ - x^-} \cos(\pi x) + A. \tag{3.2}$$

Here x is discretized equidistantly as

$$x_i = \frac{(i + \frac{1}{2})}{N + 2L},$$

with N being the number of points inside the domain, L corresponding to the number of ghost points outside the domain, and $i \in \{0; N-1\}$ being the index of the corresponding grid point. The boundaries that are at $r^+ = A+1$ and $r^- = A-1$ are at locations

$$x^+ = \cos\left(\frac{(N+L)\pi}{N+2L}\right) \quad \text{and} \quad x^- = \cos\left(\frac{L\pi}{N+2L}\right)$$

in terms of the coordinate x. Introducing $g = \frac{r^+ - r^-}{x^+ - x^-}$ and $A = \frac{r^+ + r^-}{2}$, we find for the inverse mapping

$$x = \arccos\left(\frac{r - A}{g}\right). \tag{3.3}$$

Defining metric coefficients

$$H(r) = -\frac{1}{g} \frac{1}{\sqrt{1 - \frac{r-A}{g}}} \quad \text{and} \quad G(r) = \frac{1}{g^2} \frac{\frac{r-A}{g}}{\left(1 - (\frac{r-A}{g})^2\right)^{3/2}},$$

the Laplacian in the coordinates x, θ reads

$$\nabla^2_{x,\theta} f = \left(G(r) + \frac{H(r)}{r}\right) \partial_x f + H^2(r) \partial_{xx} f + \frac{1}{r^2} \partial_{\theta\theta} f, \tag{3.4}$$

and the Jacobian transforms as

$$[a, b]_{r,\theta} = \frac{H(r)}{r} [a, b]_{x,\theta}. \tag{3.5}$$

Note that we left the dependence on r in the metric coefficients and operators. By using (3.2), however, r is readily replaced by x. Instead of the original equation (2.3)

in poloidal coordinates (r,θ), we then are able to consider the system in the new set (x,θ),

$$\frac{\partial \omega}{\partial t} + \frac{H(r)}{r}[\omega,\psi]_{x,\theta} = \nu \nabla^2_{x,\theta}\omega, \tag{3.6}$$

$$\nabla^2_{x,\theta}\psi = -\omega. \tag{3.7}$$

We thus can use the equidistant (x,θ) grid with the Arakawa discretization of the nonlinearity without experiencing more complications using a nonequidistant grid.

3.3. Boundary conditions. In the double periodic case boundary conditions are trivial. Solution of the Poisson equation (2.4), as well as the Helmholtz-type equation that arises from the implicit part of the code, is performed using Fourier modes, as this reduces inversion of the operator to a simple multiplication.

In the bounded case Fourier modes still can be used in the periodic direction. In the nonperiodic direction second order centered FDs are used to discretize the differential operators. The tridiagonal matrices appearing for each Fourier mode are then efficiently solved by pivoted Gaussian elimination.

Inferring boundary conditions on the vorticity ω from the no-slip velocities at the wall, $\nabla\psi \mid_{r=r^\pm} = (v_\theta, -v_r) \mid_{r=r^\pm} = (0,0)$, is a difficult and somewhat controversial task [10]. Here we will use the fact that our time-stepping scheme is already split between the convection part, which is explicit and thus does not need boundary information for $t_{i+1} = t_i + \Delta t$, and the implicit solution of the Helmholtz problem associated to viscosity. It is interesting to note that this is somewhat natural, since no-slip boundary conditions imply a finite viscosity. Here we use a variant of the computational boundary method (CBM) [10]: After having completed the explicit part of the time stepping we use the intermediate vorticity at the new time t^{i+1} $\tilde{\omega}^{i+1}$ to determine the azimuthal velocity $\tilde{v}_\theta^{i+1}$ at time t^{i+1}. The predicted values of $\tilde{v}_\theta^{i+1}$ include the effects of convection but miss the corrections arising from the viscosity operator. In a corrector-like step the predicted values of the poloidal velocity are then used to determine the amount of vorticity on the wall using $\tilde{v}_\theta \mid_{r=r^\pm} = 0$ for no-slip boundary conditions:

$$\tilde{\omega}^{i+1} \mid_{r=r^\pm} = -\partial_r \tilde{v}_\theta^{i+1} \mid_{r=r^\pm} .$$

These approximated boundary values are then used as boundary values for ω^{i+1} in the implicit part of the timestep. The first predictor–corrector step already converges to numerical accuracy, so iterating this scheme further does not produce any different results.

4. Spectral schemes. As described above, FD schemes are local schemes that evaluate the derivatives using values of nearby points. In the spectral approach, (2.3)–(2.4) are solved by expanding the solution into a series of orthonormal functions, resulting in a coupled system of equations for the time evolution of the expansion coefficients. We will follow the time evolution of a finite number of these coefficients. Such schemes are denoted "global," as derivatives are expressed using analytical relationships between the expansion functions. The simplest spectral scheme uses Fourier modes for each direction on a periodic domain. Such schemes are very easy to implement, partly explaining the widespread use of periodic boundary conditions in numerical simulations. As the derivative of a given Fourier mode only involves a

multiplication of that same mode, solving the Poisson, and likewise the Helmholtz, equation is trivial. Note that generally for other kinds of spectral expansions and FD schemes the Poisson operator is not diagonal and the solution is a difficult operation involving the solution of large linear systems of equations. The boundary conditions for Fourier schemes are, by nature of the expanding functions, periodic. We note that periodic boundary conditions imply zero circulation of the flow,

$$\Gamma = \int_D \omega d\mathbf{r} = -\oint_{\partial D} \nabla\Psi d\vec{S} = 0 \tag{4.1}$$

(see (2.4)).

For bounded domains an expansion into Fourier modes is not appropriate: as the periodic extension exhibits discontinuities, the Fourier expansion suffers from the Gibbs phenomenon and converges very slowly unless the solution vanishes to sufficiently high order near the boundary. In order to solve (2.3)–(2.4) in a periodic annular domain, we use a product basis comprised of Chebyshev polynomials for the radial direction and Fourier modes for the azimuthal direction,

$$g(r,\theta,t) = \sum_{m=0}^{M} \sum_{n=-N/2}^{N/2-1} g_{mn}(t)\, T_m(r)\, e^{in\theta}, \tag{4.2}$$

where M and N are the orders of truncation and $T_m(r)$ (with normalized r) is the mth degree Chebyshev polynomial. (For further information see [2, 3, 4, 6].)

For each timestep two elliptic equations, the Poisson equation (2.4) and the Helmholtz equation originating from the implicit term, must be solved. These equations are solved by an invertible integral operator method [7], which very efficiently solves the equations in $O(MN)$ operations with high accuracy even at high truncations ($M \sim N \sim 1024$). The invertible integral operator method is developed for ordinary differential equations with varying, rational function coefficients. It decomposes the solution into a particular and homogeneous solution, with the homogeneous chosen to satisfy the boundary conditions.

The no-slip boundary condition on the fluid velocity

$$\vec{u}(r^{\pm},\theta) = (0,0) \tag{4.3}$$

requires the stream function to satisfy the Neumann boundary conditions

$$\left.\frac{\partial\psi_n}{\partial r}\right|_{r^{\pm}} = 0, \tag{4.4}$$

as well as the Dirichlet boundary conditions

$$\begin{aligned} \psi_0(r^{\pm}) &= F^{\pm}(t), \\ \psi_n(r^{\pm}) &= 0\,; \quad n \neq 0, \end{aligned} \tag{4.5}$$

where $F^{\pm}(t)$ are arbitrary functions of time and n denotes the Fourier mode.

The boundary conditions (4.4) and (4.5) will cause the Poisson equation (2.4) to be overdetermined unless the $\omega_n(r)$ are restricted to ensure that both sets of conditions are fulfilled simultaneously. Although this apparent overdeterminacy can be adequately addressed by solving the ω and ψ equations simultaneously, this leads to the inversion of matrices of size $2n \times 2n$, in which the banded character of the operators of the uncoupled, constraint-based formulation is lost. An accurate and efficient

method for determining these "solvability constraints" is presented in [9, 8], and a description of how this method is adapted to annular geometry is given in [2, 6]. The result is a set of self-consistent no-slip boundary conditions

$$\left.\frac{\partial \psi_0}{\partial r}\right|_{r=r^\pm} = 0,$$

$$\psi_n(r^\pm) = 0, \qquad n \neq 0\,, \tag{4.6}$$

together with

$$\left.\frac{\partial \omega_0}{\partial r}\right|_{r=r^\pm} = 0 \tag{4.7}$$

and

$$\sum_{m=0}^{M} B^\pm_{nm}\,\omega_{nm} = 0, \qquad n \neq 0\,. \tag{4.8}$$

The constraint coefficients, $B^\pm_{nm}$, can be determined accurately and efficiently by several equivalent methods. These coefficients are independent of the value of the viscosity, ν, and they need only be calculated once for each different geometry; i.e., they depend only on the main radius, A, in addition to M and N. Values of $B^\pm_{nm}$ obtained for high values of M and/or N can be used directly in calculations with lower resolution.

In the explicit calculation of the nonlinear convection term, the products are calculated in configuration space and the result fully de-aliased using the standard 2/3 truncation scheme.

5. Results.

5.1. Doubly periodic flow. First, we present results for a doubly periodic situation. As an initial condition we start from two Gaussian-shaped monopoles with a maximum vorticity of one, half-width of $R = 0.8$, and placed 3.0 length units apart. The size of the domain is 10×10 length units. To ensure zero circulation a constant, negative vorticity $\omega_{corr} = -1/10^2 \int w_{initial} d\mathbf{r}$ has been added to the initial condition. We performed numerical simulations for local Reynolds numbers based on the maximum initial velocity $V \simeq 0.25$ and R as $Re \equiv \frac{RV}{\nu}$. The results we discuss are for two different Reynolds numbers: a moderate number of $Re = 8.000$ and a very high number of 100.000. In both cases we use resolutions of $M = N = 128, 256, 512$, and 1024. Note that the resolution will always be of the form $M = N$.

In Figure 5.1 we display the vorticity field at $T = 100.0$ for $Re = 8.000$ and $Re = 100.000$ and for all three schemes using the highest resolution. Initially, the vortices are placed so close that they merge after encircling each other for about half a rotation. In order to conserve angular momentum during the merging, fine scaled filaments are sheared off the vortices. Due to the shear flow setup of the vortex core these filaments will be continuously stretched until they reach a size where the kinematic viscosity dominates. Please consult, e.g., [20] for further information about this merging process.

For the moderate Reynolds number, $Re = 8.000$, the spectral and the Arakawa schemes produce (nearly) identical results. The position and tightness of the filaments

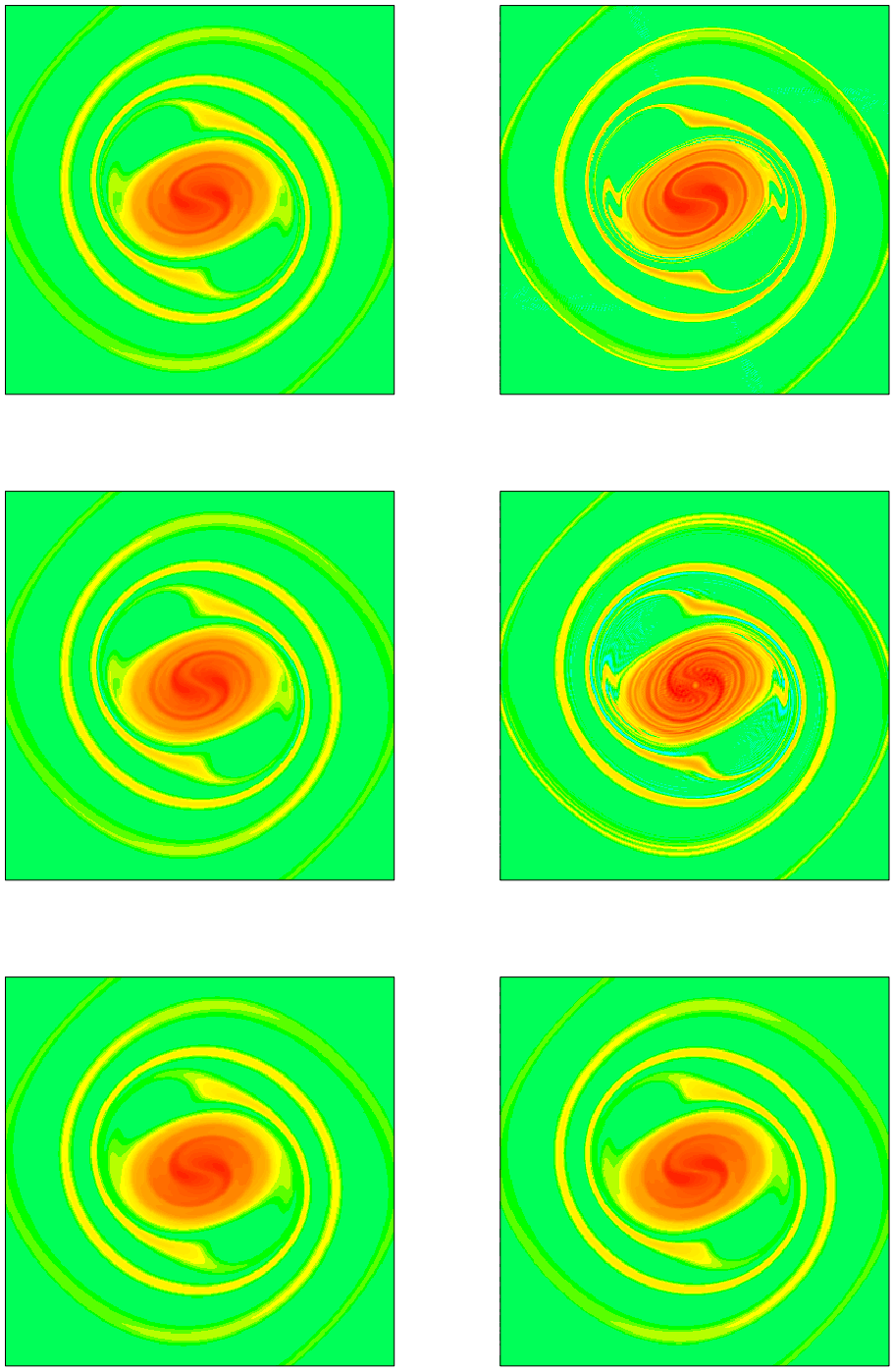

FIG. 5.1. *Vorticity at* $T = 100.0$ *for the spectral scheme (top row), Arakawa scheme (middle row), and the ENO run (bottom row). Initial condition: two Gaussian monopoles with* $Re = 8.000$ *(left column) and* $Re = 100.000$ *(right column) in a doubly periodic domain using a resolution of* $M = N = 1024$. *Note that only* 875×875 *points are shown.*

as well as the very fine spiral structure inside the compound vortex are in close agreement. The ENO scheme does, at first glance, look similar. On closer inspection it is, however, obvious that most of the fine structure has been lost. In conclusion only the larger scales are in agreement with the results obtained by the two other schemes. For high Reynolds number, $Re = 100.000$, the Arakawa scheme and the spectral scheme produce a certain amount of small scale noise, pushing the vorticity amplitude slightly above one. We do not observe this noise for the ENO scheme, as numerical viscosity is embedded into that scheme just for that reason. We observe very little difference in the resulting dynamics as described by the ENO scheme, even while increasing the Reynolds number by more than a factor of 10! In the ENO scheme—strictly limiting the vorticity amplitude—the numerical viscosity dominates over the physical effects of high Reynolds number leading to a different behavior of the fine scale filaments when compared to the Arakawa and Fourier schemes. Efficiently, the ENO scheme solves the problem for a different, resolution-dependent Reynolds number.

In Figures 5.2–5.3 we present the temporal evolution of the enstrophy and the error according to (2.11) for both Reynolds numbers. However, one should also note that the differences in time evolution can be very different in size than indicated by the error calculated from (2.11), as this reflects global quantities only. The ENO calculations are dominated by dissipative effects inherent in the scheme. Consequently the ENO scheme dissipates the more enstrophy the less resolution is used. The spectral and the Arakawa schemes show the opposite behavior, losing slightly more enstrophy with higher resolution. This is due to the fact that the higher resolution allows more enstrophy to be transported into the dissipation range at high k values. Note that in yet another class of numerical schemes this kind of behavior is modeled by introducing "eddy viscosity" (LES) to account for the dissipative effect of the scales not resolved by the numerical scheme [22].

Comparing the errors for the spectral and the Arakawa schemes shows that the Arakawa scheme, as defined, conserves energy and enstrophy in the nonlinearity and thus produces a very small error only. Due to the locality of the scheme the error improves linearly with resolution. The spectral scheme performs very well, with larger improvements in the error due to the globality of the code leading to "spectral accuracy" [4]. Both schemes additionally reproduce the dynamics of the merging dipoles with strong agreement between details of the core and the filaments.

In Table 5.1 we show the CPU time per timestep for the different schemes and for all the resolutions on an IBM RS6000-pSeries 690 computer. We observe that the Arakawa scheme is approximately three times faster than both the ENO and spectral schemes. This is independent of the resolution used here. Note that as the resolution is increased by a factor of 2 the total number of timesteps also has to be increased by a factor of 2.

The conclusion from this part of the comparison is that when solving the Navier–Stokes equations, for Reynolds numbers used in this section, schemes with internally adjusted numerical dissipation are ill suited to this task. The calculated solution due to the ENO scheme always looks smooth and well behaved but is effectively solved using some localized dissipation in space and time, which is often larger than the viscosity according to the Reynolds number. Due to this restriction we will use only the Arakawa and spectral schemes in the comparison for bounded flows, as there we introduce additional sources for inaccuracy related to the use of nonequidistant grids and the implementation of the no-slip boundary condition.

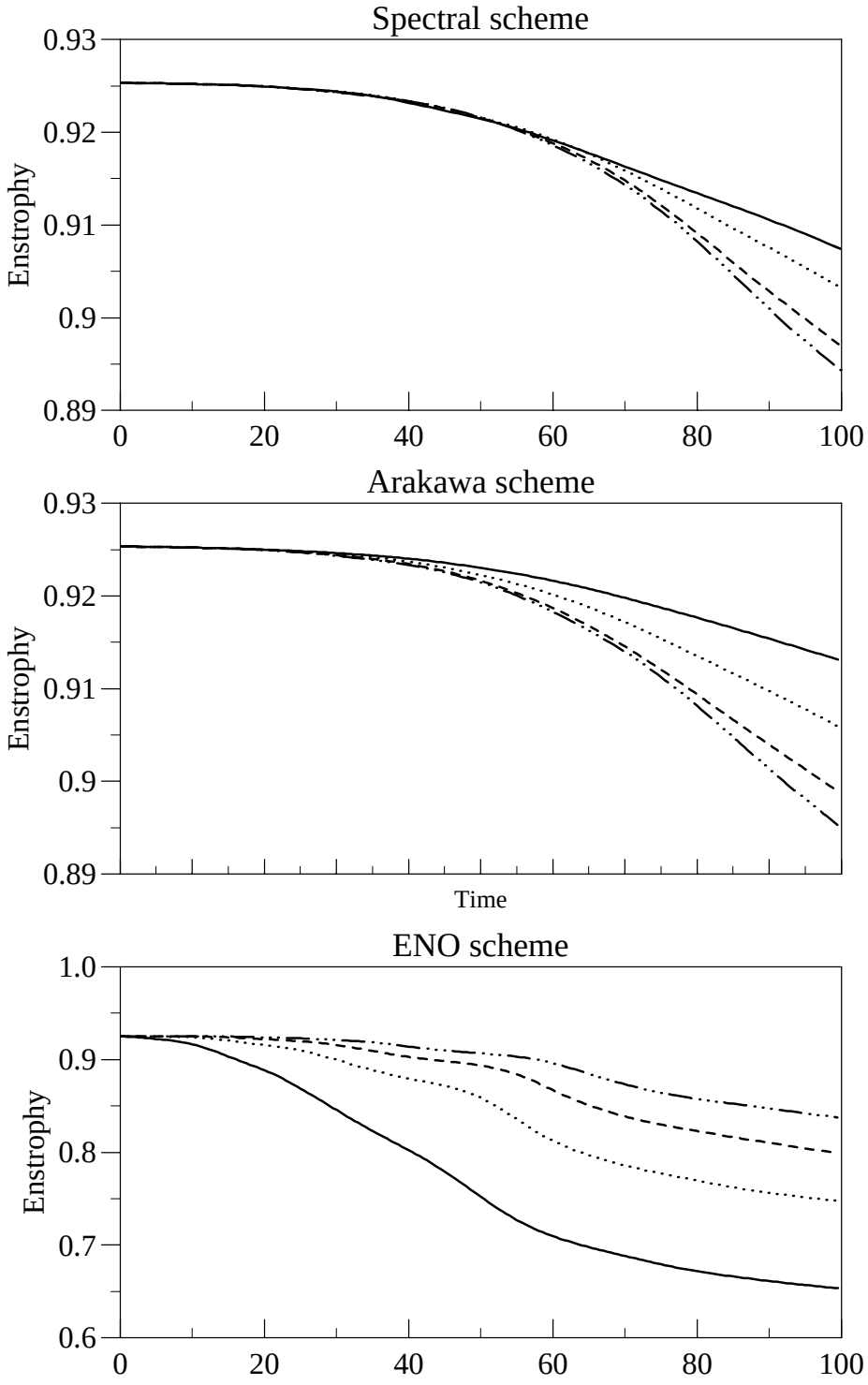

FIG. 5.2. *Time evolution of enstrophy for* $Re = 100.000$ *for the three numerical schemes in the periodic domain. Resolutions:* 128 *(solid line),* 256 *(dotted line),* 512 *(dashed line), and* 1024 *(dashed-dotted line). Note the different y-range in the last figure.*

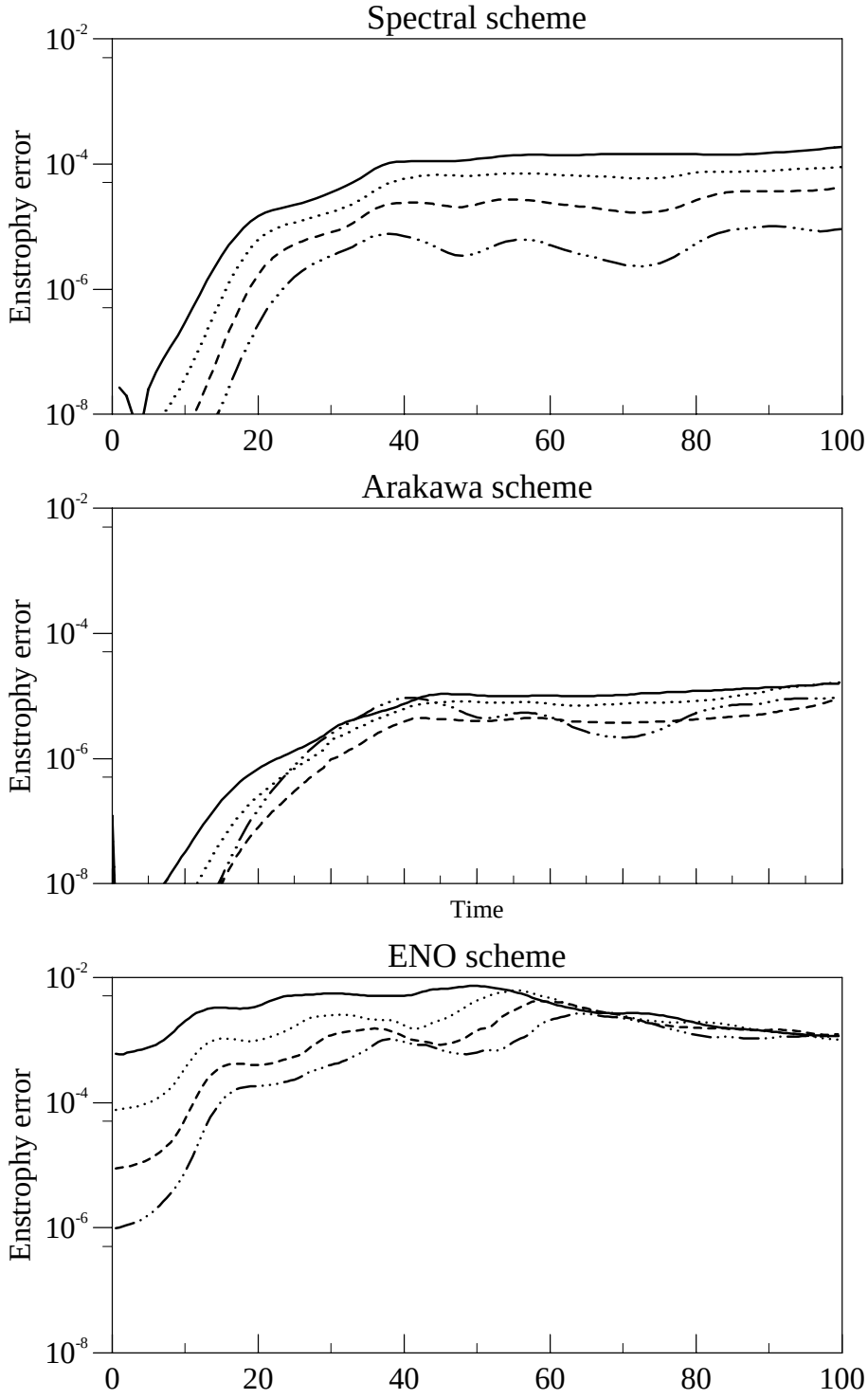

FIG. 5.3. *Time evolution of the error calculated using the vorticity and* (2.11)*, with the same parameters as in Figure* 5.2.

TABLE 5.1
CPU time per timestep for the double periodic case (rows 2–4) and the bounded case (rows 5–6).

Resolution	128	256	512	768	1024
Arakawa per.	0.003	0.012	0.068		0.332
ENO per.	0.010	0.047	0.210		0.899
Spectral per.	0.011	0.065	0.301		0.970
Arakawa ann.	0.008	0.024	0.156	0.397	0.891
Spectral ann.	0.019	0.102	0.352	0.665	1.22

5.2. Flow with no-slip boundary conditions. In this section we will study the case of flow-boundary interaction. We are considering a quarter of an annulus with inner radius of $r^- = 0.5$ and outer radius of $r^+ = 2.5$. In the azimuthal direction we employ periodic boundary conditions $\theta \in \{0; \pi/2\}$, and in the radial direction $r \in \{r^-; r^+\}$ the flow is bounded by no-slip walls.

As an initial condition we used a so-called Lamb-dipole, with the vorticity given by (see, e.g., [17] and [21])

$$\omega = \begin{cases} \frac{2\lambda U}{J_0(\lambda R)} J_1(\lambda r)\cos\theta, & r \le R, \\ 0, & r > R, \end{cases} \tag{5.1}$$

where $U = 1.0$ is the velocity of the Lamb-dipole, $R = 0.25$ is its radius, and $\lambda R = 3.831\ldots$ is the first zero of J_1. Using such a structure as an initial condition for studying complex flow-boundary interaction has several advantages. The Lamb-dipole is known to be rather stable even when exposed to strong perturbations. Due to its localized rotational interior and irrotational exterior, combined with its linear momentum, the dipole minimizes the initial boundary layer. The corresponding local Reynolds number for the Lamb-dipole is defined as $Re = UR/\nu$. For the two different numerical schemes, we have investigated their accuracy for the following Reynolds numbers: $Re = 500,\ 1000,\ 2000$, and 4000 using resolutions of $M = N = 128,\ 256,\ 512,\ 768$, and 1024.

For a given Reynolds number we initialize a Lamb-dipole in the spectral code using $M = 1024$ and integrate 100 timesteps so that any transient phenomena, especially at the boundaries, have died out. For both schemes and for all resolutions we used this relaxed state as an initial condition.

Figure 5.4 shows the time evolution for $Re = 2.000$ using the spectral Chebyshev–Fourier code with a resolution of $M = 1024$. As the dipole approaches the no-slip wall a strong boundary layer is formed. At time $t \approx 1.0$ the boundary layer splits the incoming dipole into two new dipoles, each of which consists of a strong monopole originating from the boundary vorticity and half the original dipole. The newly formed dipoles are asymmetric and their trajectory describes a circle making them collide in front of the outer wall. As can be seen from Figure 5.4 several rebounds take place, and we observe that each is associated with a significant production of vorticity at the wall. In Figure 5.5 we display the enstrophy evolution for this case and the three other Reynolds numbers considered. We observe that each rebound corresponds to a production of enstrophy with the first impact having the strongest enstrophy production. We also observe that the maximum enstrophy level is increased with increasing Reynolds number.

We have performed two different kinds of comparisons. First, for a Reynolds number of 2.000 we compared the pointwise values of the vorticity field from the spectral scheme to the FD scheme using both equidistant distributed (FDe) and cosine

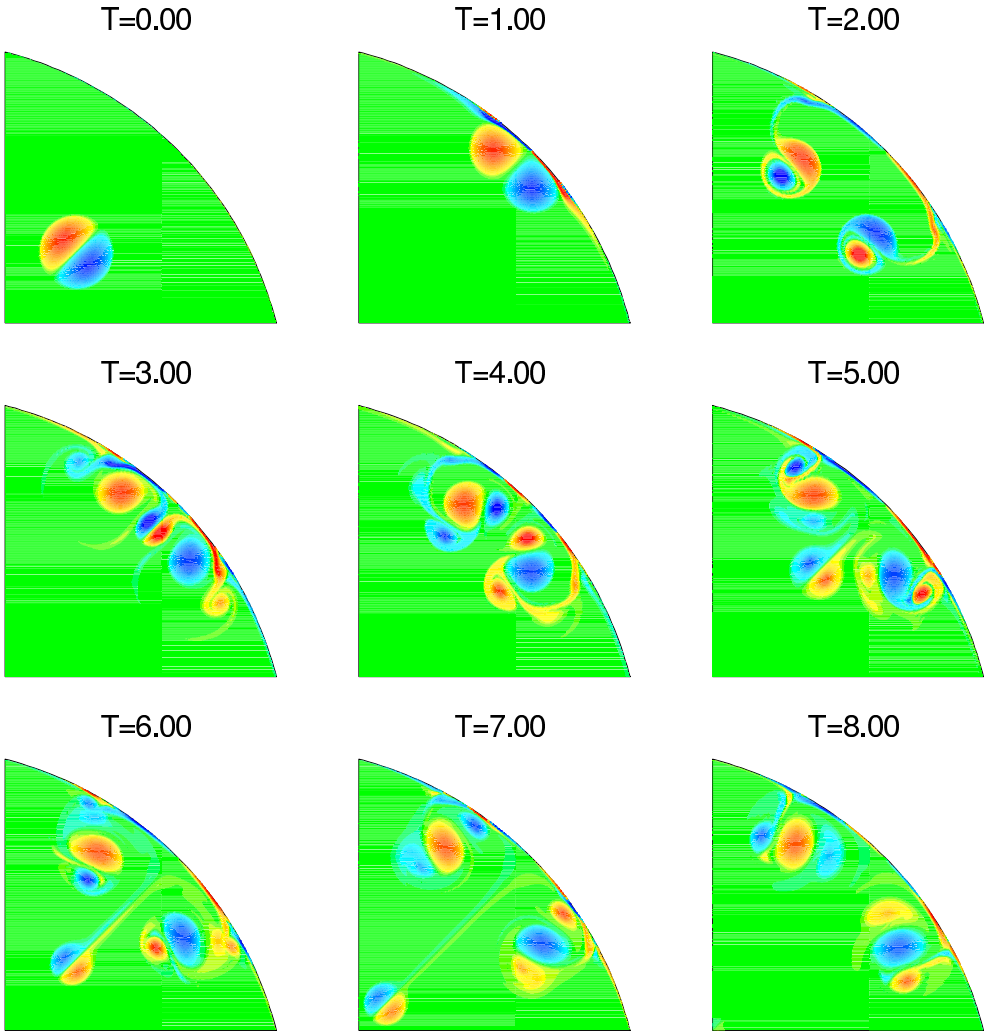

FIG. 5.4. *Time evolution of the vorticity field for the interaction of a Lamb-dipole with a no-slip wall. The spectral scheme has been used with* $M = N = 1024$ *and* $Re = 2.000$. *Notice that only a part of the computational domain is displayed.*

distributed (FDc) radial points. Second, we compared the spectral scheme to the FDc scheme using the global enstrophy evolution as a test of accuracy. We note here that the other global quantity, the energy, showed much less variation, as it reflects the larger scales more than the enstrophy.

A pointwise comparison is extremely sensitive to the path the vortices take after the collision with the wall and is therefore well suited to giving insight into the convergence of the schemes as well as their detailed accuracy.

Figure 5.6 shows the vorticity distribution in a small area near the wall for $T = 4.0$. The figure shows the results for resolutions of 512 and 1024 points and all three schemes, that is, spectral, FDe, and FDc. The time shown corresponds to the rebounce of the dipole. There are several interesting features to be observed from these figures. For the FDc the result is approximately identical to the spectral scheme using the same resolution, with nearly a one-to-one correspondence for all the contours.

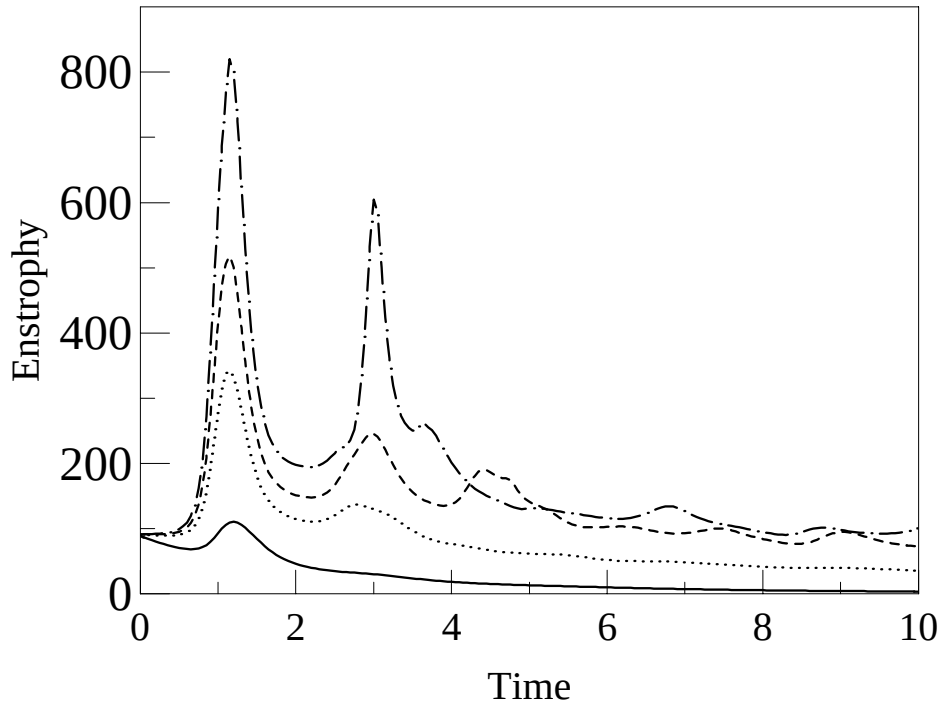

FIG. 5.5. *Time evolution of enstrophy for* $Re = 200$ *(solid line),* $Re = 1.000$ *(dotted line),* $Re = 2.000$ *(dashed line), and* $Re = 4.000$ *(dashed-dotted line) for the spectral scheme and a resolution of* $M = N = 1024$.

The differences between 512 and 1024 points of resolution are also minor for both schemes. If we, however, compare to the FDe we observe much larger differences. For a resolution of 512 points we observe an additional vortical structure, visible on the left side of the figure. Increasing the resolution to 1024 points does improve the accuracy, but a ghost of this structure can still be seen. Second, we note that the positions of the three remaining structures are not the same as the positions the two other schemes depict. Finally, a close inspection of the boundary layer shows that this layer is not resolved even with 1024 points of resolution. In general we conclude that in the chosen case we gain accuracy corresponding to a factor from 2 to 4 in resolution using the FDc compared to the FDe.

The time evolution of the vorticity at a given point, indicated by the black dot in Figure 5.6, is displayed in Figure 5.7 for resolutions 256, 512, and 1024 and all three schemes used above. It is obvious that all codes are able to calculate the propagation of the Lamb vortex correctly, as is indicated by the excellent agreement between codes as the positive part of the dipole passes between times 0.5 and 1.0. After collision with the wall the evolution of the rebouncing vortex shows great differences in the behaviors of the codes. First, it is seen that the spectral scheme at low resolution does not capture the trail of the rebouncing vortex, but the large improvement in accuracy with higher resolution leads to a good convergence of the 512 run with the 1024 run. The FDe code captures the rebouncing vortex with 512 points of resolution, but at later times. Using a resolution of 1024 increases the accuracy, but does not reach the accuracy of the 512 spectral run, but shows some features of the latter, as the little dent before the maximum value of vorticity is reached.

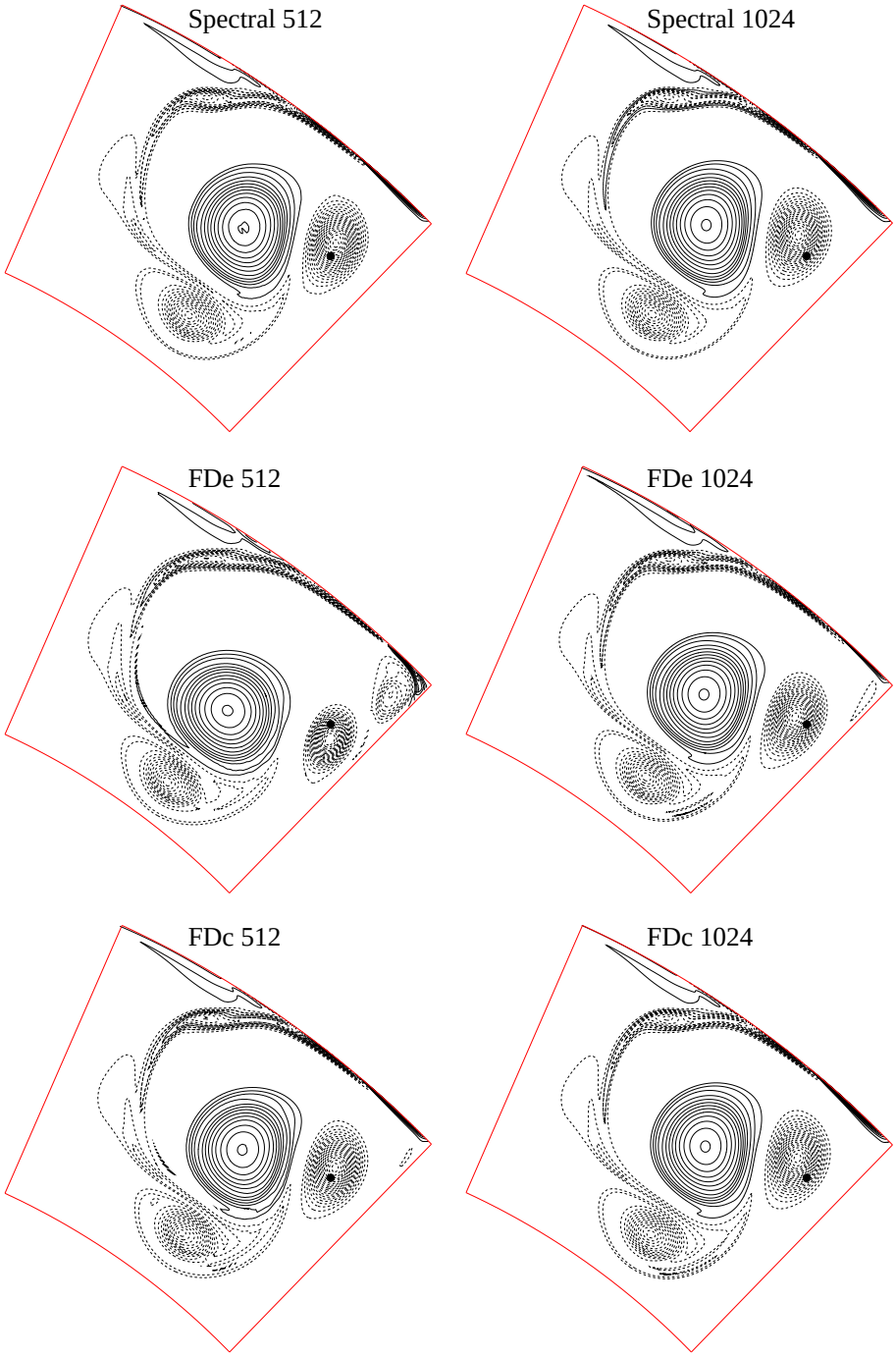

FIG. 5.6. *A close-up of vorticity contours for runs with the same parameters as in Figure* 5.4 *at* $T = 4.0$ *and* $Re = 2.000$. *Top: Spectral scheme. Middle: Arakawa scheme using an equidistant radial grid. Bottom: Arakawa scheme using cosine distributed radial grid points. Left resolution* 512 *and right resolution* 1024. *The dot in each frame locates the position where the time development is compared; see Figure* 5.7.

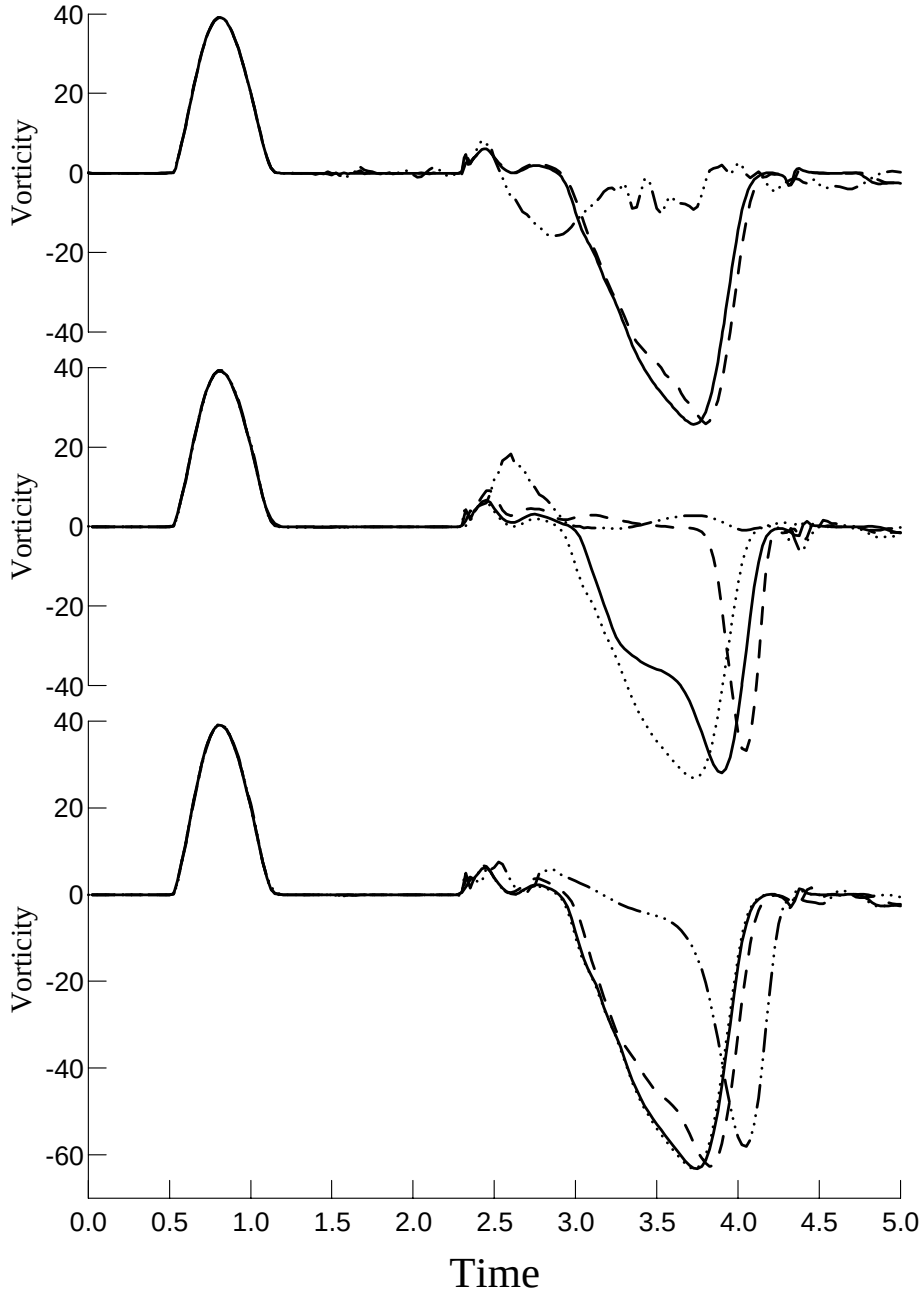

FIG. 5.7. *Time evolution of the vorticity at the point* $(r, \theta) = (2.25, 0.83)$ *(indicated by the dots in Figure* 5.6*). Top: spectral scheme. Middle: Arakawa scheme with equidistant radial grid. Bottom: Arakawa scheme with cosine distributed radial grid points. All three schemes are shown for resolutions* 1024 *(full),* 512 *(dashed), and* 256 *(dashed/dotted). The dotted lines in the two lower figures are taken for comparison from the spectral run at resolution* 1024.

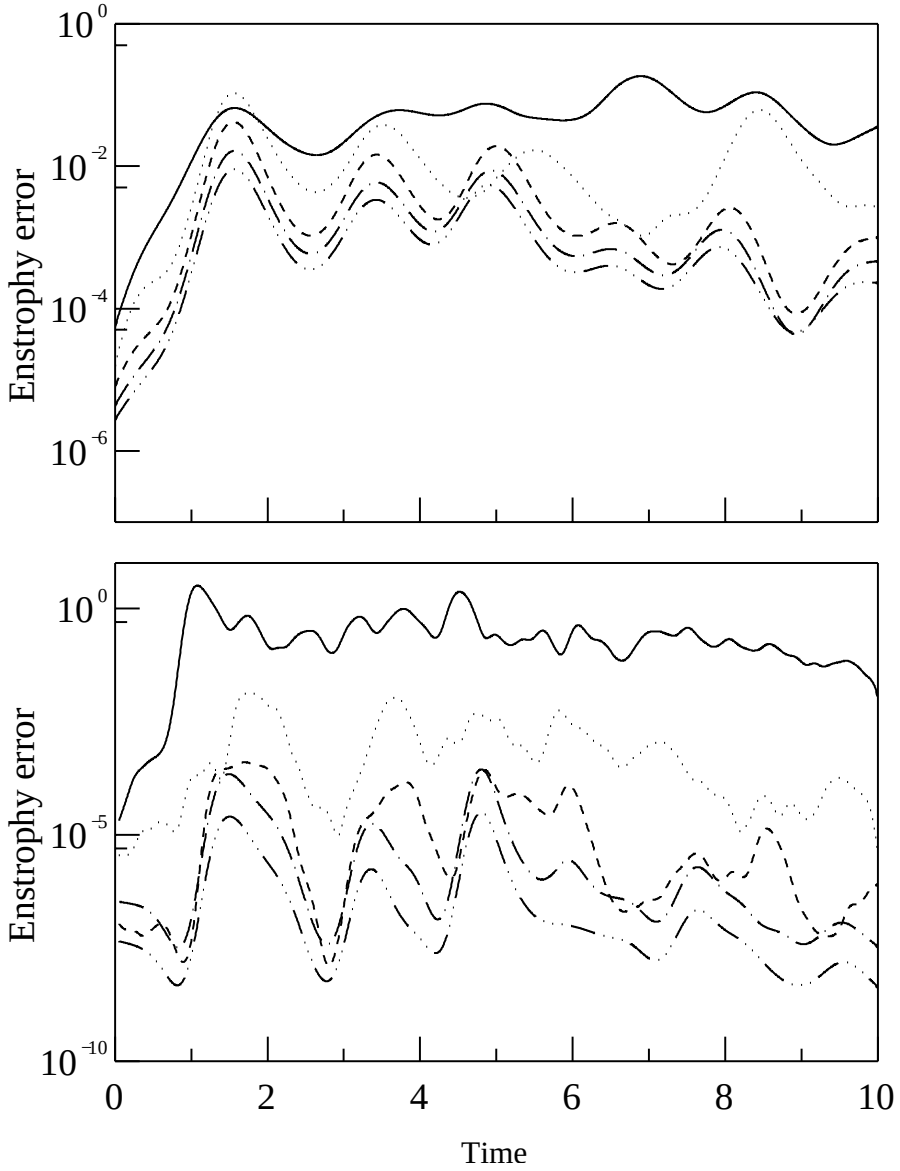

FIG. 5.8. *Time evolution of error calculated from* (2.11). *Top: FDc scheme. Bottom: spectral scheme. Schemes are shown with resolutions* 128 *(solid line),* 256 *(dotted line),* 512 *(dashed line),* 768 *(dashed-dotted line), and* 1024 *(long dotted-dashed).*

Finally the FDc performs, for a given resolution, better than the FDe run using twice the number of grid points per direction. The 512 and 1024 runs show only minor differences compared to the corresponding spectral runs, of which the 1024 run results are shown for comparison as a dotted line.

In Figure 5.8 we display the error as calculated from (2.11). For the spectral scheme, we observe that the lowest resolution, $M = 128$, has quite a large error and, when examining the vorticity, we observed that the flow field is dominated by Gibbs phenomena, i.e., by ringing. As the resolution increases, the error decreases quickly

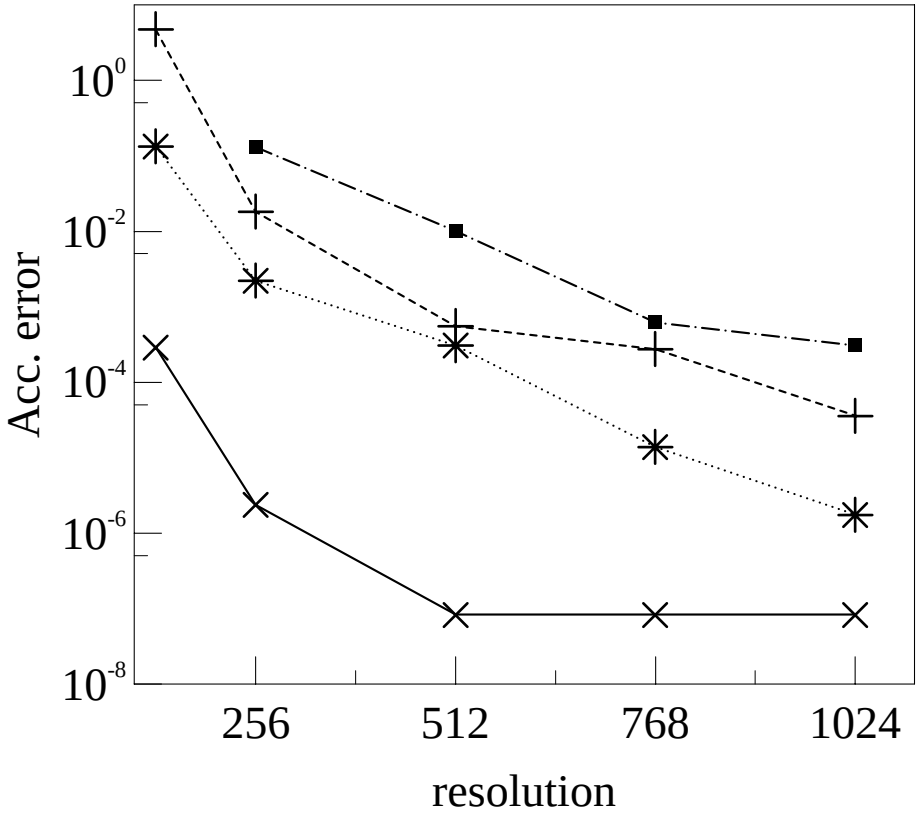

FIG. 5.9. *Integrated error calculated from* (5.2) *versus resolution for the spectral scheme. Reynolds number:* 200 *(solid line),* 1.000 *(dotted line),* 2.000 *(dashed line),* 4.000 *(dashed-dotted line).*

and the vorticity field, including the spatial position of the filaments, quickly converges as the resolution increases. For the Arakawa scheme we also observe increasing accuracy with increasing resolution, but here, as to be expected for a local scheme, the increase is much more moderate than that for the spectral schemes.

As the Reynolds number increases, the flow field becomes more and more complex and higher resolution is therefore needed. This behavior can be observed in Figures 5.9–5.10, where we display the integrated error for different Reynolds numbers and different resolutions,

$$G(Re, M) = \int_0^{t_{end}} \delta\Omega(t)dt, \tag{5.2}$$

with $t_{end} = 10.0$. In Figure 5.9 we observe the spectral convergence as the error very quickly decreases with nearly a factor of 10 as the resolution is doubled. For $Re = 200$, it saturates at a level of 10^{-7}, which reflects the accuracy of our diagnostics on the enstrophy. The simulation for $Re = 4.000$, and the resolution $M = 128$ was not possible to perform, as it became unstable.

Figure 5.10 displays the corresponding results for the Arakawa scheme. We observe again that the error decreases quickly; however, we need to quadruple the resolution in order to decrease the error by a factor of 10.

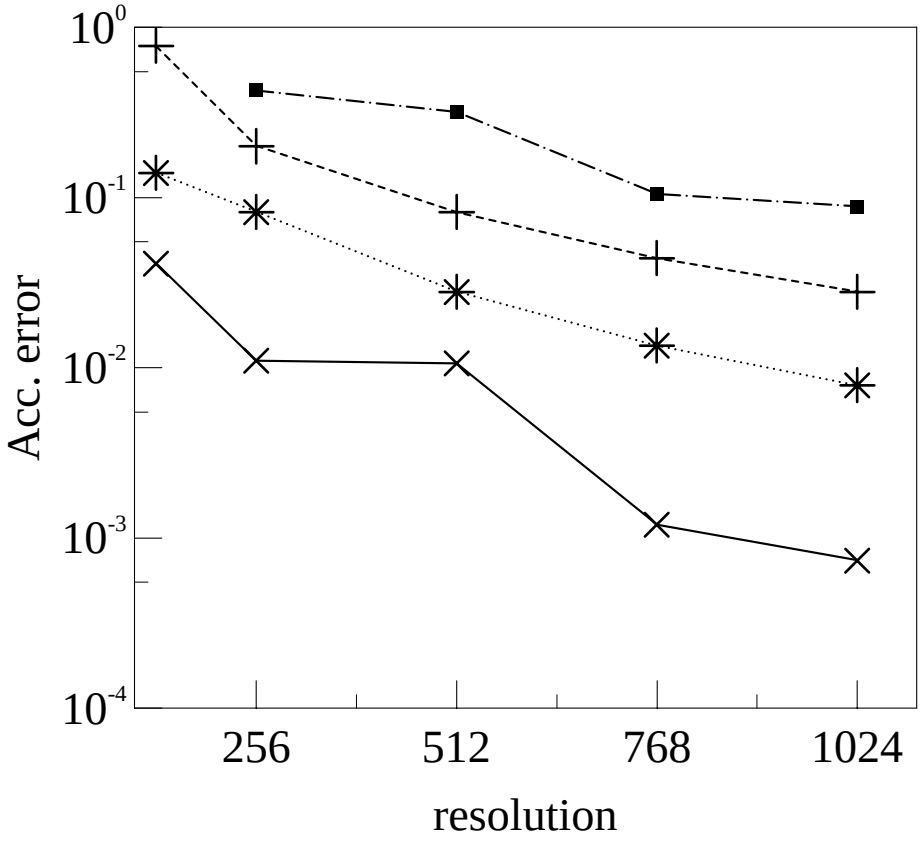

FIG. 5.10. *Integrated error calculated from* (5.2) *versus resolution for the FDc scheme. Reynolds number:* 200 *(solid line),* 1.000 *(dotted line),* 2.000 *(dashed line),* 4.000 *(dashed-dotted line).*

6. Conclusion. We have compared two FD schemes and a spectral scheme for the problem of two merging monopoles at moderate and high Reynolds numbers. We observed that the ENO scheme is dominated by internal dissipation effects and does not solve the problem for the prescribed Reynolds number. The ENO-based schemes seem to be ill suited for such high Reynolds number calculations. The schemes based on the Arakawa discretization of the nonlinearity and the Fourier spectral code, however, showed strong agreement and consistent behavior at increasing spatial resolution.

We then turned to the problem of a dipole interacting with a no-slip wall in a periodic annular domain. Here additional stress is put on the numerical scheme due to the evolution of fine structured boundary layers and the nontrivial implementation of the no-slip boundary condition. We showed that, while not reaching spectral accuracy as observed for the spectral scheme, the FD code can solve the problem with high accuracy. We note, however, that in order to obtain this high accuracy for the Arakawa scheme it is crucial to use nonequidistantly spaced grid points such as the Chebyshev collocation points. Using equidistantly distributed grid points, we obtained results with significantly lower accuracy, and needed about 2–4 times as many grid points in each direction to obtain comparable results.

In conclusion we note that for the solution of convection types of problems for a given Reynolds number it is important to reflect the conservation properties of the nonlinearities; otherwise the parameter dependence of the solution might be obscured or lost.

Finally, while FD schemes do not show spectral convergence of the overall error as spectral codes, they can nevertheless resolve the detailed dynamics of the problem. For numerical convergence it seems, however, to be more important to investigate the pointwise differences in the solutions rather than the integral error estimates.

Acknowledgments. The authors are grateful to Professor E. A. Coutsias of the Department of Mathematics and Statistics, University of New Mexico, Albuquerque, USA and to Professor J. Juul Rasmussen of the Optics and Fluid Dynamics Department, Risø National Laboratory, Denmark, for valuable discussions and comments.

REFERENCES

[1] A. Arakawa, *Computational design for long-term numerical integration of the equations of fluid motion: Two-dimensional incompressible flow. Part* I, J. Comput. Phys., 1 (1966), pp. 119–143.

[2] K. Bergeron, E. A. Coutsias, J. P. Lynov, and A. H. Nielsen, *Dynamical properties of forced shear layers in an annular geometry*, J. Fluid Mech., 402 (2000), pp. 255–289.

[3] J. Boyd, *Chebyshev and Fourier Spectral Methods*, 2nd ed., Dover, Mineola, NY, 2001.

[4] C. Canuto, M. Hussaini, A. Quarteroni, and T. Zang, *Spectral Methods in Fluid Dynamics*, Springer Series in Computational Physics, Springer-Verlag, New York, 1988.

[5] P. Colella, *Multidimensional upwind methods for hyperbolic conservation laws*, J. Comput. Phys., 87 (1990), pp. 171–200.

[6] E. A. Coutsias, K. Bergeron, J. P. Lynov, and A. H. Nielsen, *Self organization in* 2*d circular shear layers*, in Proceedings of the 25th AIAA Plasmadynamics and Lasers Conference, American Institute of Aeronautics and Astronautics, Reston, VA, 1994, p. 11.

[7] E. A. Coutsias, T. Hagstrom, and D. Torres, *An efficient spectral method for ordinary differential equations with rational function coefficients*, Math. Comp., 65 (1995), pp. 611–635.

[8] E. A. Coutsias, J. S. Hesthaven, and J. P. Lynov, *An accurate and efficient spectral tau method for the incompressible Navier–Stokes equations in a planar channel,* in Proceedings of the Third International Conference on Spectral and High Order Methods (ICOSAHOM '95), Houston Journal of Mathematics, University of Houston, Houston, TX, 1995, pp. 39–54.

[9] E. A. Coutsias and J. Lynov, *Fundamental interactions of vortical structures with boundary layers in two-dimensional flows*, Phys. D, 51 (1991), pp. 482–497.

[10] P. M. Gresho, *Incompressible fluid dynamics: Some fundamental formulation issues*, Ann. Rev. Fluid Mech., 23 (1991), pp. 413–453.

[11] A. Harten, B. Enquist, S. Osher, and S. R. Chakravarthy, *Uniformly high order accurate essentially non-oscillatory schemes,* III, J. Comput. Phys., 71 (1987), pp. 231–303.

[12] A. H. Nielsen, J. Juul Rasmussen, and V. Naulin, *Dynamics of vortex interaction in two-dimensional flows*, Phys. Scripta, T98 (2002), pp. 29–33.

[13] G. E. Karniadakis, M. Israeli, and S. A. Orszag, *High-order splitting methods for the incompressible Navier–Stokes equations*, J. Comput. Phys., 97 (1991), pp. 414–443.

[14] A. Kurganov and D. Levy, *Third-Order Semi-Discrete Central Scheme for Conservation Laws and Convection-Diffusion Equations*, Tech. Report 43528, Lawrence Berkeley National Laboratory, Berkeley, CA, 1999.

[15] A. Kurganov and D. Levy, *A third-order semidiscrete central scheme for conservation laws and convection-diffusion equations*, SIAM J. Sci. Comput., 22 (2000), pp. 1461–1488.

[16] R. LeVegue, *Numerical Methods for Conservation Laws*, Lectures in Mathematics, Birkhäuser-Verlag, Basel, 1992.

[17] V. V. Meleshko and G. J. van Heijst, *On Chaplygin's investigations of two-dimensional vortex structures in an inviscid fluid*, J. Fluid Mech., 272 (1994), pp. 157–182.

[18] R. Mittal and P. Moin, *Suitability of upwind-biased finite difference schemes for large-eddy simulation of turbulent flows*, AIAA J., 35 (1997), pp. 1415–1417.

[19] Y. Morinishi, T. Lund, O. Vasilyev, and P. Moin, *Fully conservative higher order finite difference schemes for incompressible flow*, J. Comput. Phys., 143 (1998), pp. 90–124.
[20] A. H. Nielsen, X. He, J. Juul Rasmussen, and T. Bohr, *Vortex merging and spectral cascade in two-dimensional flows*, Phys. Fluids, 8 (1996), pp. 2263–2265.
[21] A. H. Nielsen and J. Juul Rasmussen, *Formation and temporal evolution of the lamb-dipole*, Phys. Fluids, 9 (1997), pp. 982–991.
[22] H. Panofsky and J. Dutton, *Atmospheric Turbulence*, Wiley, New York, 1984.
[23] B. D. Scott, *Three dimensional computation of drift Alfvén turbulence*, Plasma Physics and Controlled Fusion, 39 (1997), pp. 1635–1668.